

## An Approach for Optimizing Prompt Gamma Photon-Based Range Estimation in Proton Therapy Using Cramér-Rao Theory

Lens, Eelco; Tolboom, Ellen; Schaart, Dennis

**DOI**

[10.1109/TRPMS.2019.2921634](https://doi.org/10.1109/TRPMS.2019.2921634)

**Publication date**

2019

**Document Version**

Final published version

**Published in**

IEEE Transactions on Radiation and Plasma Medical Sciences

**Citation (APA)**

Lens, E., Tolboom, E., & Schaart, D. (2019). An Approach for Optimizing Prompt Gamma Photon-Based Range Estimation in Proton Therapy Using Cramér-Rao Theory. *IEEE Transactions on Radiation and Plasma Medical Sciences*, 4(2), 161-169. Article 8733086. <https://doi.org/10.1109/TRPMS.2019.2921634>

**Important note**

To cite this publication, please use the final published version (if applicable). Please check the document version above.

**Copyright**

Other than for strictly personal use, it is not permitted to download, forward or distribute the text or part of it, without the consent of the author(s) and/or copyright holder(s), unless the work is under an open content license such as Creative Commons.

**Takedown policy**

Please contact us and provide details if you believe this document breaches copyrights. We will remove access to the work immediately and investigate your claim.

# An Approach for Optimizing Prompt Gamma Photon-Based Range Estimation in Proton Therapy Using Cramér-Rao Theory

E. Lens, E. Tolboom, and D.R. Schaart, *Member IEEE*

**Abstract**— Various methods for *in vivo* range estimation during proton therapy based on the measurement of prompt gamma (PG) photons have been proposed. However, optimizing the method of detection by trial-and-error is a tedious endeavor. Here, we investigate the feasibility of using the Cramér-Rao lower bound (CRLB) to more quickly arrive at an optimum detector design. The CRLB provides the smallest possible variance on the proton range obtained from any unbiased estimator, given a statistical model of the observations.

We simulated clinical proton pencil beams targeting a cylindrical, soft-tissue equivalent phantom and scored the PG photons around the phantom. Spatially, temporally and spectrally resolved PG emission profiles corresponding to different proton ranges were generated. We calculated the proton range estimation uncertainty as a function of several detector setup parameters such as detector size, bin size, and photon acceptance angle.

We found a minimum uncertainty for the proton range estimation based on either spatial, spectral, or temporal information of 2.13 mm, 1.97 mm and 2.05 mm, respectively, if the detection parameters were optimized for each case.

We conclude that the CRLB is a promising tool for the optimization of the detector setup for PG based range estimation in particle therapy.

**Index Terms**— Prompt gamma photon detection, proton therapy, Cramér-Rao theory, detector optimization, Monte Carlo simulations.

This study was financially supported by ZonMw, the Netherlands Organization for Health Research and Development, grant number 104003012 and by Varian Medical Systems. The calculation time on the SURFsara Lisa system was granted by NWO Physical Sciences.

E. Lens and E. Tolboom are with the Radiation Science and Technology Department, Delft university of Technology, Delft, The Netherlands.

D.R. Schaart is with the Radiation Science and Technology Department, Delft university of Technology, Delft, The Netherlands and with the Holland Proton Therapy Center, Delft, The Netherlands. D.R. Schaart is the corresponding author (e-mail: [d.r.schaart@tudelft.nl](mailto:d.r.schaart@tudelft.nl)).

## I. INTRODUCTION

With the growing use of proton therapy worldwide, there is also an increasing interest in state-of-the-art quality assurance to ensure patient safety and treatment quality. Because of the highly localized dose deposition of individual pencil beams, a small geometric uncertainty (e.g. a small anatomical change) or an incorrect proton range prediction can greatly impact the dose distribution [1]. An important form of quality assurance for proton therapy is real-time treatment monitoring based on the detection of secondary photons generated by nuclear

interactions of the incoming protons with the elements that make up the patient. These photons can be either annihilation photons that are the result of generated positron emitters, or prompt gamma (PG) photons that are directly emitted by excited nuclei returning to the ground state [2], [3]. The detection of these secondary photons could also be applied in an adaptive treatment setting. The measured signal would then be used to obtain information about deviations in the treatment due to, for example, day-to-day anatomical variations or an incorrect proton range prediction and, where needed, to adapt the treatment.

Annihilation photons are typically measured using conventional positron emission tomography (PET) detector systems by transporting the patient to such a system after irradiation or with newly developed in-room PET systems [4], [5]. The detection of PG photons has to be done during radiation delivery since the emission occurs essentially instantaneously (within  $< 1$  ns) [6]. The energy of the PG photons that can be observed in clinical proton therapy are typically in the order of 1.0–7.5 MeV [7]. Different properties of the detected PG photons have been shown to carry information on the proton range. Properties such as: the location of detection of the photon on the detector (i.e. spatial information), the energy of the detected photon (i.e. spectral information) or the time of arrival/detection (i.e. temporal information) [8]–[11]. Regardless of what technique is being used, extensive studies are often needed in order to optimize the detector system.

Different detector systems have been described and reported to be successful in detecting PG photons and using the data for range verification during proton therapy, all with different measurement techniques, detector systems, and methods of analysis [3], [7]–[10], [12]–[36]. These studies describe different detector setups, detection limits, and factors that could influence the obtained results.

Typical detector setup parameters that affect the results are: detector size, detector location, bin size, and energy resolution. In addition, a typical PG photon detection system also requires a collimator to obtain spatial information from the incoming photons, the design of this collimator also greatly impacts the measurement results. For example, large slit widths result in more counts on the detector but reduce the spatial resolution. Such trade-offs are typically of great interest since these determine the final performance of the system.

The optimization of detector systems can e.g. be done using Monte Carlo simulations, sweeping through the parameter

space and analyzing which system results in prompt gamma signals that provide the best resolution on the proton range. An example of such a trial-and-error study is the work from Pinto *et al.* where an impressive total number of 14730 different collimator geometries were simulated [14].

A different and potentially more efficient approach to optimize detector systems is to apply Cramér-Rao theory, which allows for the calculation of the lower bound on the variance of any unbiased estimator of a parameter of interest (e.g. the proton range) as a function of the different detector setup parameters. The calculation of this Cramér-Rao lower bound (CRLB) requires a statistical model of the data. The CRLB thus offers a convenient way of optimizing detector systems without having to run the large number of simulations. Cramér-Rao theory has been shown to be useful in similar cases where it was used to optimize the detector design of PET systems and to determine the limits on the spatial and time resolutions of such systems [37]–[39].

The aim of this work is to illustrate the application of Cramér-Rao theory for the optimization of detector systems that are to be used for the estimation of the proton range in an irradiated medium based on the measurement of prompt gamma signals. Three simple Monte Carlo simulations were performed to obtain the required data and from there a full detector optimization could be performed, regardless of which information was taken from the photons (i.e. spatial, spectral or temporal information). The proposed method allows for a characterization of how the accuracy of a detector system depends on the setup parameters and helps to better understand the influence of specific setup parameters on the measurement results.

## II. MATERIALS AND METHODS

### A. Cramér-Rao Lower Bound Formalism

The CRLB is based on the Cramér-Rao inequality [40] and can be used to find the theoretical lower bound on the variance of any unbiased estimator of a parameter, given a statistical model of the observables. This work focuses on determining the proton range ( $R$ ) from the detected prompt gamma (PG) signals. The PG photons are generated in the irradiated medium at the nuclear interaction sites between the incoming protons and the nuclei of the medium. Next, the photons are detected in a detector system outside the irradiated medium. The information contained by the photons can be subdivided into spatial, spectral and temporal information. All three types of information can be considered as giving rise to a 1-dimensional (1D) observable in the detector system, that could be used to determine  $R$ . In the following we illustrate the CRLB formalism when using the spatial information of the measured PG photons to determine  $R$ ; for the spectral and temporal observables, the derivations are similar.

The measurement area (i.e. detector) is one-dimensionally subdivided into  $i$  bins along the beam axis and each bin detects  $n_i$  photons. The number of detected photons per bin scales with the number of protons and thus, in extension, with the total number of emitted photons ( $N_\gamma$ ) and its expectation value can

be written as the product of  $N_\gamma$  and the fraction  $f_i(R)$  of photons that reaches bin  $i$ . The fraction  $f_i(R)$  is dependent on  $R$  since the proton range determines the number of emitted photons that reach a certain bin. The expectation value for the number of detected photons in a bin  $i$  is given by:

$$E[n_i] = N_\gamma \cdot f_i(R). \quad (1)$$

The emission and detection process of the PG photons can be described by Poisson statistics, resulting in a probability  $p_i$  to detect  $n_i$  photons in bin  $i$  (given  $R$  and  $N_\gamma$ ):

$$p_i(n_i|R, N_\gamma) = \frac{(N_\gamma \cdot f_i(R))^{n_i}}{n_i!} \cdot e^{-N_\gamma \cdot f_i(R)}. \quad (2)$$

It is noted that (2) ignores the influence of the variance of  $N_\gamma$  on  $n_i$ . Since  $N_\gamma \gg 1$  and  $f_i(R) \ll 1$  in a typical clinical PG detection setup, this can be considered a valid approximation in most cases of practical interest.

It follows that the likelihood to detect  $\bar{n} = (n_1, n_2, \dots, n_p)^T$  photons in the  $P$  detector bins is given by:

$$L(\bar{n}|R, N_\gamma) = \prod_{i=1}^P p_i(n_i|R, N_\gamma). \quad (3)$$

Using this likelihood function, we can define the Fisher information matrix:

$$\mathbf{M} = -E \left[ \frac{\partial^2 \ln(L(\bar{n}|R, N_\gamma))}{\partial R^2} \right], \quad (4)$$

where  $E$  gives the expectation value. Combining (3) and (4) and following the steps from [37], the Fisher matrix can be written as (see Appendix):

$$\begin{aligned} \mathbf{M} &= N_\gamma \cdot \sum_{i=1}^P \frac{1}{f_i(R)} \frac{df_i(R)}{dR} \frac{df_i(R)}{dR} \\ &= N_\gamma \cdot \sum_{i=1}^P \frac{1}{f_i(R)} \left( \frac{df_i(R)}{dR} \right)^2. \end{aligned} \quad (5)$$

The term  $\left( \frac{df_i(R)}{dR} \right)^2$  results from the fact that we are dealing with a 1D problem where we are only interested in estimating the proton range  $R$ . The lower bound  $\mathbf{M}^{-1}$  on the variance of an unbiased estimator now follows from the Cramér-Rao inequality:

$$\text{cov}(\hat{R}, \hat{R}) = \text{var}(\hat{R}) \geq \mathbf{M}^{-1}, \quad (6)$$

where  $\hat{R}$  is the estimated value of the proton range  $R$ .

The lower bound on this variance can now be calculated by evaluating the Fisher information matrix at  $\hat{R}$ . The smallest possible uncertainty in the estimated proton range ( $\sigma_R$ ) can then be calculated by taking the square root of the calculated smallest possible variance of the estimated proton range:

$$\sigma_R = \sqrt{\text{var}(\hat{R})}. \quad (7)$$

As mentioned before, the preceding derivation holds for all three of the proposed 1D PG photon observables: spatial information on a 1D detector as well as spectral and temporal information. For the last two observables, the detector bins  $i$  simply correspond with the energy and the time of arrival of the detected photon, respectively, regardless of the position on the detector where the photon was detected.

It is emphasized once more that the CRLB provides the lower bound on the uncertainty of the estimated range shift for *any* unbiased estimator. In this work, we will not elaborate on the various methods currently being investigated for estimating range shifts from experimentally obtained PG signals (either spatial, spectral or temporal). Obviously, the accuracy achieved in practice may be different for different methods and some methods may approach the lower bound more closely than others. That is, in statistical terms, some methods may be more *efficient* than others. Thus, the CRLB is also useful for quantifying the efficiency of different estimators.

In order to calculate  $\sigma_R$ , the derivative  $\frac{df_i(R)}{dR}$  (see (5)) must be known. This derivative can be approximated by the numerical derivative:

$$\frac{df_i(R)}{dR} = \frac{f_i(R+h) - f_i(R-h)}{2h} + O(h^2), \quad (8)$$

where the higher order terms were neglected. This numerical derivative can be calculated straightforwardly using Monte Carlo simulations.

In this study we assumed that the PG photon emission process is covered by Poisson statistics and because the photon detection process is a binomial selection of  $N_\gamma$ ,  $n_i$  also follows a Poisson distribution. We can therefore express the variance of  $n_i$  as:

$$\text{var}(n_i) = \langle N_\gamma \rangle f_i(R). \quad (9)$$

Where  $\langle N_\gamma \rangle f_i(R)$  is the mean number of photons measured by bin  $i$ . In addition, the covariance between different bins is expressed by [40]:

$$\text{cov}(n_i, n_j) = \langle N_\gamma \rangle f_i(R) \delta_{i,j}, \quad (10)$$

where  $\delta_{i,j}$  is the Kronecker's delta function. Therefore, the covariance between different bins is zero and the covariance of a bin is equal to its variance. A non-zero covariance between bins (i.e. pixels) could, for example, be caused if an incoming high-energy PG photon would scatter multiple times in the detector, giving rise to crosstalk and therefore a signal in multiple pixels.

### B. Monte Carlo Simulations

In order to obtain the dataset that could be used to calculate the fractions  $f_i(R)$  as well as the derivative given in (8) we

performed Monte Carlo simulations. The simulations were performed using the TOPAS (version 3.1.p1) (Geant4 10.3.p01 based) Monte Carlo code [41] and were performed on the Dutch national computing cluster LISA (SURFsara, Amsterdam, the Netherlands). The default physics list was used, which has been shown to yield similar results for proton therapy research as the earlier suggested Geant4 physics lists [42]. Since this work aims to provide a first demonstration of how Cramér-Rao theory can be applied for detector optimization when using detected PG photons for proton range verification, neutrons were excluded in the simulations.

The geometry that was simulated consisted of a cylindrical phantom with a radius of 100 mm and a length of 300 mm. The material was made out of ICRU-soft-tissue-4. This is a predefined material ( $\rho = 1.0 \text{ g/cm}^3$ ) in TOPAS that consists of 10.12% hydrogen, 11.10% carbon, 2.60% nitrogen and 76.18% oxygen, the four most abundant elements in the human body and the ones that produce the majority of the PG photons [7]. The phantom was irradiated with a mono-energetic proton beam and the resulting PG photons were scored on a coaxially placed cylinder with a radius of 400 mm and a maximum length of 800 mm. Fig. 1 shows a schematic illustration of the experimental setup that was used in the simulations.

The proton range that was used to calculate the CRLB values was 150.0 mm. To be able to calculate the derivatives given by (8) we performed three simulations with different proton energies corresponding to a predefined proton range of 150.0 mm, 149.5 mm and 150.5 mm ( $R$  and  $R \pm h$ ). The corresponding proton energies were: 146.208 MeV, 145.930 MeV and 146.487 MeV, respectively. For each energy we simulated  $4 \times 10^9$  protons, each time using a different random seed, resulting in a  $N_\gamma$  of  $\pm 6.3 \times 10^8$ . Since the PG emission process is dependent on the cross sections for the nuclear interactions, each simulation resulted in a slightly different  $N_\gamma$ . The value of  $h$  should ideally be as small as possible (see (8)). However, if  $h$  would be too small, the noise in  $f_i(R)$  would become a limiting factor. The currently chosen value of 0.5 mm was the smallest value that resulted in an acceptable noise level in the simulated PG signals within the available calculation time and in combination with the smallest spatial bin size of 1.0 mm that was used (Table I).

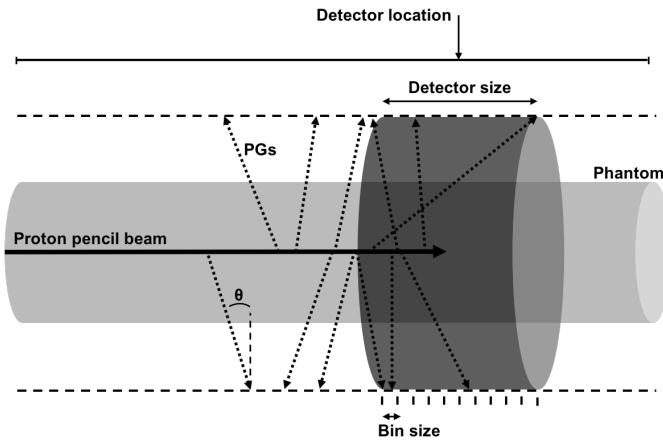


Fig. 1. Schematic of the setup used in the Monte Carlo simulations. The figure illustrates the definitions of the prompt gamma (PG) photon angle of incidence ( $\theta$ ), the detector size, the detector location (centered around the proton range in this example; location is 0 mm) and the bin size.

### C. Optimization of Detector Setup/Parameters

To illustrate the optimization process of a PG detection setup using the CRLB, we investigated the influence of the different detection setup parameters shown in Fig. 1, while measuring different properties of the incoming PG photons: position of detection (spatial distribution), photon energy (spectral distribution) and time of arrival (temporal distribution).

For each combination of setup parameters studied, we plotted the detected profiles for range  $R$  and  $R \pm h$ . Next, we plotted the derivative as given in (8). This plot already indicates where the information is located in the measured data; if the derivative has a nonzero value at a certain point, then there is a change in the measured profile due to the range shift ( $h$ ) and this change could be exploited to detect the range shift. From the derivative we calculated the Fischer information matrix according to (5) and plotted the  $\frac{1}{f_i(R)} \left( \frac{df_i(R)}{dR} \right)^2$  term from (5). The resulting plot gives a more accurate indication of the information density since it is corrected for the signal strength at each bin.

The resulting CRLB values will be calculated using (7) and this was done using a number of protons per pencil beam that is comparable to what can be expected in actual treatment plans. The average number of protons in a clinical pencil beam used in a prostate treatment is between  $10^7$ – $10^8$  [43]. In this study, we calculated the CRLB values for a pencil beam with  $6.0 \times 10^7$  protons, which can be considered as the average pencil beam intensity in a prostate treatment [44].

#### Spatial Information of the PG Photons

We were only interested in the spatial distribution of the photons along the beam axis, since 1D intensity profiles are typically measured when using PG emission for proton range verification. A partial ring with a certain size of the detection cylinder was used (i.e. the ring only covers part of the phantom in the longitudinal direction) as PG photon detector and this detector was divided into ring-shaped bins with a certain width (Fig. 1). For measurements of 1D intensity profiles along the beam axis, e.g. a multi-slit collimator can be used. Such a collimator was simulated by discriminating the photons on

angle of incidence ( $\theta$ ).

Optimization of the detector was simulated by varying the detector size, bin size, and acceptance angle. The latter was done to simulate different types of multi-slit collimator, which would affect the acceptance angle. The ranges of values used for the different parameters are given in Table I. The energy cut-off was set to 0 MeV, i.e. no energy discrimination was applied, and the detector was always centered at the proton range  $R$ , which is referred to as a detector location of 0 mm.

#### Spectral Information of the PG Photons

For this part, we considered the entire detector surface as a single spatial bin and we only used the spectral information of the incoming photons. Again, we changed different parameters in order to simulate different detection setups. We varied the acceptance angle, energy resolution, and detector size (Table I). The energy resolution was modeled as a Gaussian blur of the spectrum with an energy-dependent full-width-at-half-maximum of:  $\text{FWHM} = \frac{\text{res}(\%) \cdot E}{\sqrt{E}}$ ; where  $\text{res}(\%)$  is the value used for the scintillator energy resolution. Again, no energy cut-off was applied and the detector was centered around the proton range. The energy of the detected photons is typically detected at a continuous scale, but in this study, we binned the energy, after applying the blurring, with a bin size of 0.01 MeV in order to calculate the CRLB.

TABLE I  
DETECTOR SETUP PARAMETERS

	Spatial	Spectral	Temporal
Detector size (mm)	1.0–600.0	1.0–600.0	1.0–600.0
Spatial bin size (mm)	0.001–40.0	NA	NA
Angle of acceptance ( $^\circ$ )	0.01–90.0	0.01–9.0	NA
Detector location (mm) <sup>1</sup>	0	0	-700.0–700.0
Energy resolution (%) <sup>2</sup>	NA	1–50	NA
Energy cut-off (MeV)	0	0	0
Proton bunch width (ns) <sup>3</sup>	NA	NA	1.0–2.5

Abbreviations: NA = not applicable.

<sup>1</sup>A location of 0 mm means that the detector is centered around the proton range  $R$ , while a negative value means proximal to  $R$ .

<sup>2</sup>The energy resolution was modeled as a Gaussian blur of the spectrum with an energy dependent full width at half maximum of:  $\text{FWHM} = \frac{\text{res}(\%) \cdot E}{\sqrt{E}}$ .

<sup>3</sup>FWHM of the Gaussian shaped proton bunch.

#### Temporal Information of the PG Photons

To use the temporal information of the PG photons for the detection of proton range shifts we again considered the detector as a single spatial bin and we varied the detector size, detector location, and the proton bunch width (Table I). The latter was done to investigate the influence of different proton bunch widths, as could be observed at different proton treatment clinics. That is, cyclotron-based treatment facilities deliver the protons in bunches, typically having a width in the order of ns, with a period of  $\sim 10$  ns or more in between two subsequent bunches. Thus, the protons in a single bunch do not all enter the patient at the same time, whereas in the Monte Carlo simulation, all protons start at  $t=0$ . Therefore, to simulate the influence of different bunch widths, the arrival time of the detected PG photons was blurred with a Gaussian with a

variable FWHM. The time of arrival of the detected photons is typically detected at a continuous scale, but in this study, we binned the time of arrival with a bin size of 0.01 ns in order to calculate the CRLB.

### III. RESULTS AND DISCUSSION

#### A. Detector Optimization

Figure 2 shows an example of the detected PG emission profile when using the spatial information of the detected photons, including the derivative and the normalized elements of  $M$ . Figure 3 and 4 show the profiles when using the spectral or temporal information of the detected photons. For each possible combination of detector parameters, such a figure could be generated and the  $\sigma_R$  calculated. The values plotted in Fig. 2–4 were normalized to the maximum value per curve to improve the readability of these figures.

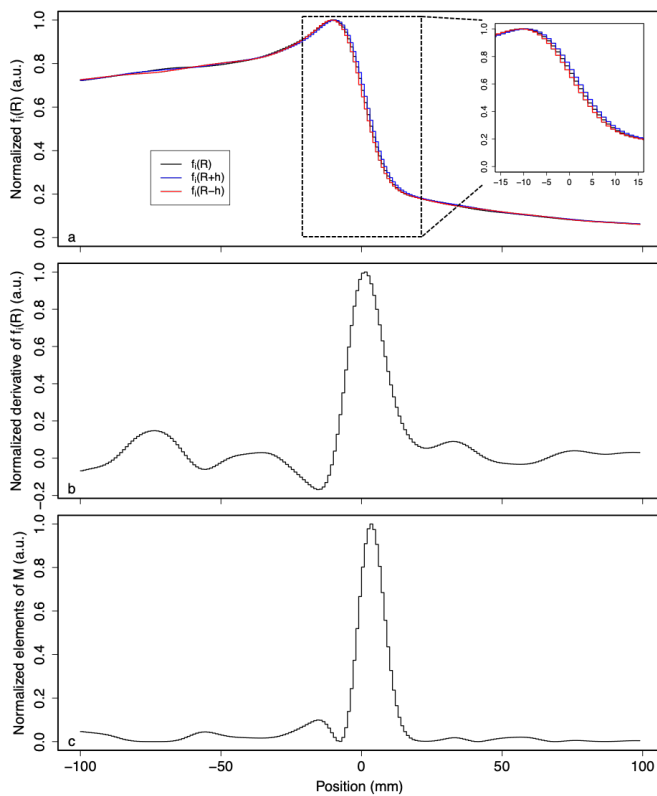


Fig. 2. (a) measured spatial prompt gamma profiles for three different proton ranges ( $R$  and  $R \pm h$ ); (b) the derivative of this signal with respect to the proton range; and (c) the normalized elements of the Fisher information matrix. The latter curve indicates the information density as a function of the location on the detector. In this example, a 200 mm detector was used that was centered around the proton range  $R$  and had a spatial bin size of 1 mm and an acceptance angle of  $0.03^\circ$ .

By fixing all parameters except one, we investigated the  $\sigma_R$  dependence on the detector setup parameters. Figure 5 shows the  $\sigma_R$  as a function of the photon acceptance angle and detector size of a system that uses the spatial information of the detected PG photons to determine the proton range. There is a relatively broad optimum for the acceptance angle (Fig. 5a), resulting from a trade-off between spatial resolution and number of detected photons. That is, the  $\sigma_R$  has a high value for

very small angles (e.g.  $0.03^\circ$ ), where the number of detected photons is low and, therefore, the relative variance is high. When increasing the acceptance angle, the number of detected photons increases and the  $\sigma_R$  improves until it reaches its minimum value. When increasing the angle even further, spatial information is lost and the  $\sigma_R$  grows larger again. In a realistic detector system, the acceptance angle could e.g. be changed by altering the slit width of the collimator. For a varying detector size (Fig. 5b), we see a continuously improving  $\sigma_R$  for larger detectors. However, after a certain point no new information is gained by increasing the detector size and the  $\sigma_R$  reaches a plateau.

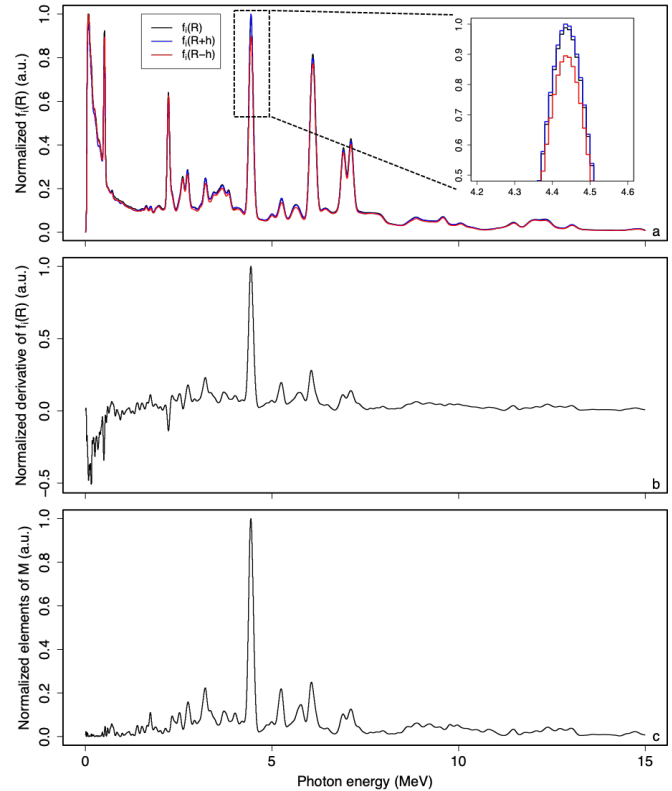


Fig. 3. (a) measured prompt gamma energy spectra for three different proton ranges ( $R$  and  $R \pm h$ ); (b) the derivative of the signal with respect to the proton range; and (c) the normalized elements of the Fisher information matrix. The latter curve indicates the information density as a function of the photon energy. In this example, a 10 mm detector was used that was centered around the proton range ( $R$ ) and had an energy resolution of 5% and an acceptance angle of  $1.5^\circ$ .

Figure 6 shows the  $\sigma_R$  as a function of acceptance angle and detector size when only using the energy of the detected PG photons. In this case, there were no individual spatial bins since all detected photons were accumulated into a single energy spectrum. For a 10 mm wide detector centered around the proton range, there is a clear optimum for the photon acceptance angle (Fig. 6a). The small optimal value ( $<2^\circ$ ) ensured that only PG photons generated by protons near the proton range were detected and this resulted in the lowest  $\sigma_R$ . For larger acceptance angles, PG photons that were generated prior to the proton range were also detected and this increased the  $\sigma_R$  since these photons dilute the information contained in the spectrum. The same holds for the  $\sigma_R$  as a function of detector size (Fig.

6b). When the detector becomes too large, photons generated proximal to the proton range are detected, increasing the  $\sigma_R$ .

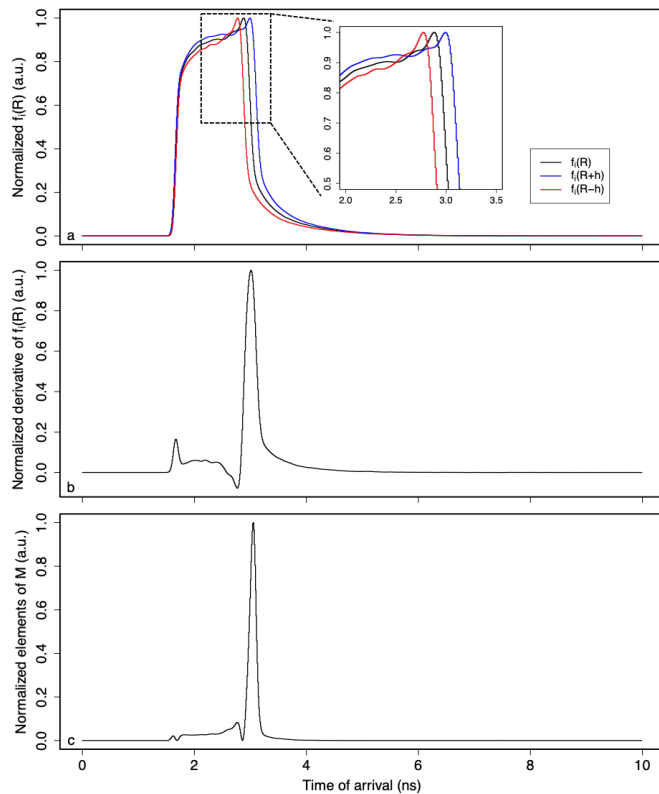


Fig. 4. (a) time-of-flight measurement of the prompt gamma photons for three different proton ranges ( $R$  and  $R \pm h$ ); (b) the derivative of the signal with respect to the proton range; and (c) the normalized elements of the Fisher information matrix. The latter curve indicates the information density as a function of the time-of-flight. In this example, a 200 mm detector was used that was centered around the proton range ( $R$ ) and the proton bunch had an FWHM of 1 ns.

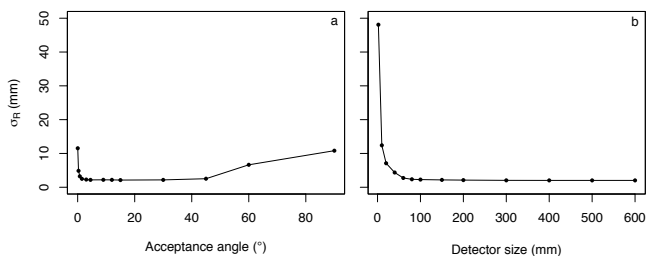


Fig. 5.  $\sigma_R$  value as a function of (a) acceptance angle and (b) detector size when using (only) the spatial information of the prompt gamma photons. In the example shown in (a), a 400 mm wide detector was used that was centered around the proton range  $R$  and had a spatial bin size of 10 mm. In the example shown in (b), a detector was used that was centered around the proton range  $R$  and had a spatial bin size of 0.5 mm and an acceptance angle of  $3^\circ$ .

Figure 7 shows the  $\sigma_R$  as a function of detector location and size when using the time-of-flight of the detected PG photons. It can be beneficial to position the detector proximal to the proton range, as the lowest  $\sigma_R$  was obtained for a detector positioned at -300 mm (Fig. 7a). By placing the detector at this position, the differences in absolute distance that photons generated at different positions along the proton track have to travel to the detector is increased and this results in better

differentiation between the photons and thus better resolution. The  $\sigma_R$  as a function of detector size is continuously improving with increasing detector size when the detector is positioned 300 mm proximal to  $R$  (Fig. 7b). For small detectors the detection efficiency is reduced, hence the smaller  $\sigma_R$  values.

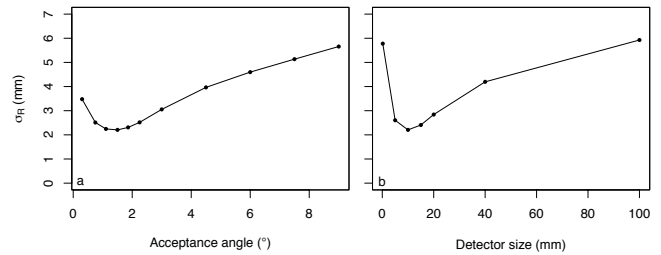


Fig. 6.  $\sigma_R$  value as a function of (a) acceptance angle and (b) detector size when using the energy information of the prompt gamma photons. In the example shown in (a), a 10 mm wide detector was used that was centered around the proton range  $R$  and had an energy resolution of 5%. In the example shown in (b), a detector was used that was centered around the proton range  $R$  and had an acceptance angle of  $3^\circ$  and an energy resolution of 5%.

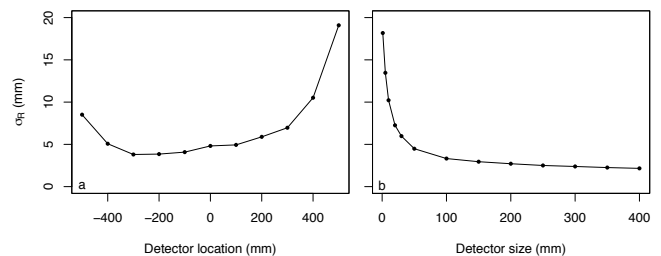


Fig. 7.  $\sigma_R$  values as a function of (a) detector location and (b) detector size when using the time-of-flight of the prompt gamma photons. In the example shown in (a), a 50 mm wide detector was used and the proton bunch width was 1 ns FWHM. In the example shown in (b), the detector was placed 300 mm proximal to the proton range  $R$  (i.e. a location of -300 mm) and the proton bunch width was 1 ns FWHM.

The smallest  $\sigma_R$  that were found when using either the spatial, spectral, or temporal information of the detected PG photons are shown in Table II. Interestingly, these values are highly comparable, indicating that similar performance could be achieved, provided that the optimum setup parameters listed in the table are used in each case. The choice of what photon information is to be used can thus be made based on the available detectors and/or other practical considerations. For the energy resolution of the detector and the proton bunch width, the smallest  $\sigma_R$  would be achieved for the smallest possible value of these parameters (i.e. perfect energy resolution and a proton bunch width value of 0 ns). In this study, the minimum values of these parameters were fixed based on realistic values (Table II). If the energy resolution were decreased from 5% to 50%,  $\sigma_R$  would increase with  $\pm 10\%$ . For the proton bunch width this effect is more pronounced, increasing the proton bunch width from 1 ns to 2 ns already increases  $\sigma_R$  with  $\pm 130\%$ .

TABLE II

SMALLEST OBTAINED UNCERTAINTIES FOR THE ESTIMATED PROTON RANGE OF A SINGLE 146 MeV PENCIL BEAM CONTAINING  $6.0 \times 10^7$  PROTONS

	Spatial	Spectral	Temporal
Detector size (mm)	600.0	10.0	600.0
Bin size (mm)	12.5	NA	NA
Angle of acceptance (°)	9.0	1.5	NA
Detector location (mm) <sup>1</sup>	0	2.0	-300
Energy resolution (%) <sup>2,3</sup>	NA	5.0	NA
Proton bunch width (ns) <sup>4,5</sup>	NA	NA	1.0
$\sigma_R$ (mm)	2.13	1.97	2.05

Abbreviations: NA = not applicable.

<sup>1</sup>A location of 0 mm means that the detector is centered around the proton range  $R$  and a negative value means proximal to  $R$ .

<sup>2</sup>The energy resolution was modeled as a Gaussian blur of the spectrum with an energy dependent full width at half maximum of:  $\text{FWHM} = \frac{\text{res}(\%) \cdot E}{\sqrt{E}}$ .

<sup>3</sup>A better energy resolution will always result in lower  $\sigma_R$  values and the value of 5% was based on the finite resolution of realistic scintillation detectors.

<sup>4</sup>FWHM of the Gaussian shaped proton bunch.

<sup>5</sup>A smaller proton bunch width will always result in lower  $\sigma_R$  values and the value of 1.0 ns was based on the actual clinical proton bunch width [10].

<sup>6</sup>Smallest possible uncertainty on the estimated proton range  $R$ .

### B. Limitations of the Model

The current study aims to introduce and demonstrate the use of Cramér-Rao theory as a tool for the optimization of detector systems and range estimators. The CRLB model presented in section II.A was therefore kept simple. In particular, we assumed that the measured PG signal (either spatial, spectral or temporal) varies with the proton range  $R$  only. Since PG photon emission is a stochastic process, the number of emitted PG photons  $N_\gamma$  actually has a finite variance. The influence thereof was neglected in equation (2), under the assumption that  $N_\gamma \gg 1$  and  $f_i(R) \ll 1$  in typical clinical setups. It is furthermore noted the expectation value of  $N_\gamma$  could vary with  $R$ , e.g. due to changes in the elemental composition of the tissues traversed by the beam during different treatment fractions. When calculating the lower bound on the proton range estimation accuracy of a given detector system, one should consider if the variation in  $N_\gamma$  and its non-zero covariance with  $R$  need to be included in the model.

Furthermore, we used a simple cylindrical simulation geometry. It should be noted that different geometries, material compositions, etcetera, can result in a different optimal detector design and different CRLB values. It is also noted that the calculated optimal values for the smallest possible uncertainties in the estimated proton range ( $\sigma_R$ ), which were in the order of 2 mm for a single 146 MeV pencil beam containing  $6.0 \times 10^7$  protons (Table II), may not always be achievable in a real-life clinical system. This is due to the fact that an idealized detection system in terms of detection efficiency was assumed in the current study, meaning that every photon that reached the detector and had an angle of incidence smaller than the acceptance angle was detected (i.e. a detection efficiency of 100%).

In addition, all neutrons that reached the detector surface were rejected and not considered during analysis. When performing real-life PG measurements, the neutrons generated by the proton irradiation are likely to give a background signal that may influence the results, even though this background can

partially be suppressed using e.g. time-of-flight rejection [10]. The effectiveness of the suppression of such background signals using time-of-flight rejection depends heavily on what particle accelerator is used, for example a cyclotron allows for more efficient suppression compared to when a synchrotron is used.

Nevertheless, the detector performance and neutron background signal are not expected to fundamentally change the observed trends for the  $\sigma_R$  values as a function of the investigated parameters. This is because these sources of uncertainty typically give a flat background signal and thus reduce the contrast-to-noise ratio, but do not change the nature and shape of the PG emission profile. Moreover, the proposed procedure allows for the inclusion of a finite detection efficiency and/or background neutrons if needed.

The smallest possible uncertainty on the estimated proton range is proportional to the square root of the number of detected PG photons, and thus to the square root of the number of protons in the pencil beam. In this study, we used an average number of  $6.0 \times 10^7$  protons to calculate the CRLB, but clinically this value will vary per pencil beam depending on its intensity. In addition, a real clinical PG detector system typically has a planar detector surface instead of the ring-shaped surface used in this study. The cylindrical detector shape was used to maximize the PG photon count. A planar detector with a smaller surface will reduce the photon count and increase the corresponding CRLB values.

Finally, we only investigated changes in the proton range, while in clinical daily practice other causes of signal change may also occur. The proposed method can be used to detect any change in the PG emission profiles since such changes always give a non-zero value for the derivative of the signal. However, other types of signal changes might result in a different optimized detector setup and this has not been included in this work.

### C. Outlook

The procedure could be extended to the situation where two types of information are combined. For example, for each photon in a spatial bin, the energy or time of arrival could be determined simultaneously and the combined information could be used for range verification. In addition, a different model than Poisson statistics could be used and the covariance between different bins could be included. This would allow for the detector optimization while considering different types of radiation sources.

Other factors such as detection efficiency, background irradiation or what type of scintillation crystal is used, might have an even greater impact on the system performance than the parameters investigated in this work. Nevertheless, any detector parameter could be included in the Monte Carlo model and its effects studied using the CRLB.

If the complete detector response and geometry of a given detector is correctly modeled in the Monte Carlo simulation or retrospectively added to the obtained signal, the Cramér-Rao theory can be used to calculate the actual limits on the uncertainty of the proton range that could be determined with

that detector. Thus, the results can also be used as an objective benchmark for the efficiency of the estimator used to derive the proton range from the detector signals.

A clinical PG detector system would be used to monitor complete treatment plans, which typically contain proton pencil beams with varying energies. As the system performance could change with the proton energy, due to the fact that the PG photon emission is dependent on the proton energy, different proton energies could result in different optimal detector setups. This should be considered when designing a clinical PG detector system that is to be used for treatment verification.

#### IV. CONCLUSION

With this work we illustrated how Cramér-Rao theory can be applied to optimize detector systems that could be used to detect prompt gamma signals, which in turn can be used to perform range verification during proton therapy. The presented approach can be applied regardless of whether spatial, spectral, and/or temporal information is used to determine the range. It was shown that with the current simplified preliminary detector setup, the same accuracy could be achieved when using either type of information for proton range verification. However, in order to obtain more realistic numerical values for the lower bound on the variance of the estimated proton range, detailed modelling of realistic detector systems is to be performed. Using the Cramér-Rao lower bound allows for the objective optimization of such clinical PG photon detection systems and could in the future be used to simplify this process considerably.

#### APPENDIX

The Fisher information matrix as given in (5) can be obtained by combining (1)–(4). The derivation is shown in this appendix. We start substituting our definition of the likelihood function (3) in the Fisher information matrix (4) so that we obtain:

$$\begin{aligned} \mathbf{M} &= -\mathbb{E} \left[ \frac{\partial^2 \ln(L(\bar{n}|R, N_\gamma))}{\partial R^2} \right] \\ &= -\mathbb{E} \left[ \frac{\partial^2 \sum_{i=1}^P \ln(p_i(n_i|R, N_\gamma))}{\partial R^2} \right]. \end{aligned}$$

Taking the first derivative of the likelihood gives:

$$\mathbf{M} = -\mathbb{E} \left[ \sum_{i=1}^P \frac{\partial}{\partial R} \left( \frac{1}{p_i(n_i|R, N_\gamma)} \frac{\partial p_i(n_i|R, N_\gamma)}{\partial R} \right) \right].$$

Taking the derivative of  $p_i(n_i|R, N_\gamma)$  with respect to  $R$  gives:

$$\begin{aligned} \frac{\partial p_i(n_i|R, N_\gamma)}{\partial R} &= \frac{N_\gamma^{n_i}}{n_i!} \left( \frac{n_i f_i(R)^{n_i}}{f_i(R)} \frac{\partial f_i(R)}{\partial R} e^{-N_\gamma f_i(R)} \right. \\ &\quad \left. - N_\gamma f_i(R)^{n_i} \frac{\partial f_i(R)}{\partial R} e^{-N_\gamma f_i(R)} \right) \\ &= \frac{\partial f_i(R)}{\partial R} p_i(n_i|R, N_\gamma) \left( \frac{n_i}{f_i(R)} - N_\gamma \right). \end{aligned}$$

This can now be substituted in the Fisher matrix again:

$$\mathbf{M} = -\mathbb{E} \left[ \sum_{i=1}^P \frac{\partial}{\partial R} \left( \frac{\partial f_i(R)}{\partial R} \left( \frac{n_i}{f_i(R)} - N_\gamma \right) \right) \right].$$

Now taking the second derivative with respect to  $R$  leads to:

$$\mathbf{M} = -\mathbb{E} \left[ \sum_{i=1}^P \left( \frac{n_i}{f_i(R)} \frac{\partial^2 f_i(R)}{\partial R^2} - \left( \frac{\partial f_i(R)}{\partial R} \right)^2 \frac{n_i}{f_i(R)^2} - N_\gamma \frac{\partial^2 f_i(R)}{\partial R^2} \right) \right].$$

If we substitute the expectation value of  $n_i$  given in (1) we obtain:

$$\mathbf{M} = \sum_{i=1}^P \left( \frac{\partial f_i(R)}{\partial R} \right)^2 \frac{N_\gamma}{f_i(R)} = N_\gamma \cdot \sum_{i=1}^P \frac{1}{f_i(R)} \left( \frac{df_i(R)}{dR} \right)^2,$$

which is equal to (5).

#### REFERENCES

- [1] H. Paganetti, "Range uncertainties in proton therapy and the role of Monte Carlo simulations," *Phys. Med. Biol.*, vol. 57, no. 11, pp. R99–R117, 2012.
- [2] K. Parodi, F. Pönisch, and W. Enghardt, "Experimental study on the feasibility of in-beam PET for accurate monitoring of proton therapy," *IEEE Trans. Nucl. Sci.*, vol. 52, no. 3, pp. 778–786, 2005.
- [3] C. H. Min, C. H. Kim, M. Y. Youn, and J. W. Kim, "Prompt gamma measurements for locating the dose falloff region in the proton therapy," *Appl. Phys. Lett.*, vol. 89, no. 18, pp. 2–5, 2006.
- [4] P. Crespo, G. Shakirin, and W. Enghardt, "On the detector arrangement for in-beam PET for hadron therapy monitoring," *Phys. Med. Biol.*, vol. 51, no. 9, pp. 2143–2163, 2006.
- [5] E. Yoshida *et al.*, "Development of a Whole-Body Dual Ring OpenPET for in-Beam PET," *IEEE Trans. Radiat. Plasma Med. Sci.*, vol. 1, no. 4, pp. 293–300, 2017.
- [6] B. Kozlovsky, R. J. Murphy, and R. Ramaty, "Nuclear Deexcitation Gamma-Ray Lines from Accelerated Particle Interactions," *Astrophys. J. Suppl. Ser.*, vol. 141, no. 2, pp. 523–541, 2002.
- [7] J. M. Verburg, H. A. Shih, and J. Seco, "Simulation of prompt gamma-ray emission during proton radiotherapy," *Phys. Med. Biol.*, vol. 57, no. 17, pp. 5459–5472, 2012.
- [8] J. M. Verburg and J. Seco, "Proton range verification through prompt gamma-ray spectroscopy," *Phys. Med. Biol.*, vol. 59, no. 23, pp. 7089–7106, 2014.
- [9] C. Golnik *et al.*, "Range assessment in particle therapy based on prompt  $\gamma$ -ray timing measurements," *Phys. Med. Biol.*, vol. 59, no. 18, pp. 5399–5422, 2014.
- [10] P. Cambraia Lopes *et al.*, "Time-resolved imaging of prompt-gamma rays for proton range verification using a knife-edge slit camera based on digital photon counters," *Phys. Med. Biol.*, vol. 60, no. 15, pp. 6063–6085, 2015.
- [11] P. Cambraia Lopes, P. Crespo, J. Huizenga, and D. R.

- Schaart, "Optimization of the Signal-to-Background Ratio in Prompt Gamma Imaging Using Energy and Shifting Time-of-Flight Discrimination: Experiments With a Scanning Parallel-Slit Collimator," *IEEE Trans. Radiat. Plasma Med. Sci.*, vol. 2, no. 5, pp. 510–519, 2018.
- [12] F. Janssen *et al.*, "Factors influencing the accuracy of beam range estimation in proton therapy using prompt gamma emission.," *Phys. Med. Biol.*, vol. 59, no. 15, pp. 4427–41, 2014.
- [13] M. Testa, C. H. Min, J. M. Verburg, J. Schümann, H.-M. Lu, and H. Paganetti, "Range verification of passively scattered proton beams based on prompt gamma time patterns," *Phys. Med. Biol.*, vol. 59, no. 15, pp. 4181–4195, 2014.
- [14] M. Pinto *et al.*, "Design optimisation of a TOF-based collimated camera prototype for online hadrontherapy monitoring.," *Phys. Med. Biol.*, vol. 59, no. 24, pp. 7653–7674, 2014.
- [15] M. Priegnitz *et al.*, "Measurement of prompt gamma profiles in inhomogeneous targets with a knife-edge slit camera during proton irradiation," *Phys. Med. Biol.*, vol. 60, no. 12, pp. 4849–4871, 2015.
- [16] M. Priegnitz *et al.*, "Detection of mixed-range proton pencil beams with a prompt gamma slit camera," *Phys. Med. Biol.*, vol. 61, no. 2, pp. 855–871, 2016.
- [17] S. Schmid *et al.*, "Monte Carlo study on the sensitivity of prompt gamma imaging to proton range variations due to interfractional changes in prostate cancer patients," *Phys. Med. Biol.*, vol. 60, no. 24, pp. 9329–9347, 2015.
- [18] R. Alarcon *et al.*, "Detectors for in vivo range and dose verification in proton therapy," *Int. J. Mod. Phys. Conf. Ser.*, vol. 44, p. 1660217, 2016.
- [19] E. Hilaire, D. Sarrut, F. Peyrin, and V. Maxim, "Proton therapy monitoring by Compton imaging: influence of the large energy spectrum of the prompt- $\gamma$  radiation," *Phys. Med. Biol.*, vol. 61, no. 8, pp. 3127–3146, 2016.
- [20] G. Janssens *et al.*, "Sensitivity study of prompt gamma imaging of scanned beam proton therapy in heterogeneous anatomies," *Radiother. Oncol.*, vol. 118, no. 3, pp. 562–567, 2016.
- [21] H.-H. Lin, H.-T. Chang, T.-C. Chao, and K.-S. Chuang, "A comparison of two prompt gamma imaging techniques with collimator-based cameras for range verification in proton therapy," *Radiat. Phys. Chem.*, vol. 137, pp. 144–150, 2017.
- [22] C. Richter *et al.*, "First clinical application of a prompt gamma based in vivo proton range verification system," *Radiother. Oncol.*, vol. 118, no. 2, pp. 232–237, 2016.
- [23] A. Schumann, M. Priegnitz, S. Schoene, W. Enghardt, H. Rohling, and F. Fiedler, "From prompt gamma distribution to dose: a novel approach combining an evolutionary algorithm and filtering based on Gaussian-powerlaw convolutions," *Phys. Med. Biol.*, vol. 61, no. 19, pp. 6919–6934, 2016.
- [24] J. Smeets *et al.*, "Experimental Comparison of Knife-Edge and Multi-Parallel Slit Collimators for Prompt Gamma Imaging of Proton Pencil Beams," *Radiat. Oncol.*, vol. 6, p. 156, 2016.
- [25] F. Hueso-Gonzalez, G. Pausch, J. Petzoldt, K. E. Romer, and W. Enghardt, "Prompt Gamma Rays Detected With a BGO Block Compton Camera Reveal Range Deviations of Therapeutic Proton Beams," *IEEE Trans. Radiat. Plasma Med. Sci.*, vol. 1, no. 1, pp. 76–86, 2017.
- [26] M. Zarifi, S. Guatelli, D. Bolst, B. Hutton, A. Rosenfeld, and Y. Qi, "Characterization of prompt gamma-ray emission with respect to the Bragg peak for proton beam range verification: A Monte Carlo study," *Phys. Medica*, vol. 33, pp. 197–206, 2017.
- [27] L. Kelleter *et al.*, "Spectroscopic study of prompt-gamma emission for range verification in proton therapy," *Phys. Medica*, vol. 34, pp. 7–17, 2017.
- [28] L. Nenoff *et al.*, "Sensitivity of a prompt-gamma slit-camera to detect range shifts for proton treatment verification," *Radiother. Oncol.*, vol. 125, no. 3, pp. 534–540, 2017.
- [29] Y. Xie *et al.*, "Prompt Gamma Imaging for In Vivo Range Verification of Pencil Beam Scanning Proton Therapy," *Int. J. Radiat. Oncol.*, vol. 99, no. 1, pp. 210–218, 2017.
- [30] E. Draeger *et al.*, "3D prompt gamma imaging for proton beam range verification," *Phys. Med. Biol.*, vol. 63, no. 3, p. 035019, 2018.
- [31] P. Cambraia Lopes, P. Crespo, H. Simões, R. Ferreira Marques, K. Parodi, and D. R. Schaart, "Simulation of proton range monitoring in an anthropomorphic phantom using multi-slat collimators and time-of-flight detection of prompt-gamma quanta," *Phys. Medica*, vol. 54, pp. 1–14, 2018.
- [32] C. H. Min, H. R. Lee, C. H. Kim, and S. B. Lee, "Development of array-type prompt gamma measurement system for in vivo range verification in proton therapy.," *Med. Phys.*, vol. 39, no. 4, pp. 2100–2107, 2012.
- [33] A. K. Biegun *et al.*, "Time-of-flight neutron rejection to improve prompt gamma imaging for proton range verification: a simulation study," *Phys. Med. Biol.*, vol. 57, no. 20, pp. 6429–6444, 2012.
- [34] M. Moteabbed, S. Espana, H. Paganetti, S. España, and H. Paganetti, "Monte Carlo patient study on the comparison of prompt gamma and PET imaging for range verification in proton therapy," *Phys. Med. Biol.*, vol. 56, no. 4, pp. 1063–1082, 2011.
- [35] J. M. Verburg, K. Riley, T. Bortfeld, and J. Seco, "Energy- and time-resolved detection of prompt gamma-rays for proton range verification.," *Phys. Med. Biol.*, vol. 58, no. 20, pp. L37-49, 2013.
- [36] P. Gueth *et al.*, "Machine learning-based patient specific prompt-gamma dose monitoring in proton therapy.," *Phys. Med. Biol.*, vol. 58, no. 13, pp. 4563–77, 2013.
- [37] D. J. van der Laan, M. C. Maas, D. R. Schaart, P. Bruyndonckx, S. Leonard, and C. W. E. van Eijk, "Using Cramer-Rao theory combined with Monte Carlo simulations for the optimization of monolithic scintillator PET detectors," *IEEE Trans. Nucl. Sci.*,

- vol. 53, no. 3, pp. 1063–1070, 2006.
- [38] D. J. Van Der Laan, M. C. Maas, P. Bruyndonckx, and D. R. Schaart, “Limits on the spatial resolution of monolithic scintillators read out by APD arrays,” *Phys. Med. Biol.*, vol. 57, no. 20, pp. 6479–6496, 2012.
- [39] S. Seifert, H. T. van Dam, and D. R. Schaart, “The lower bound on the timing resolution of scintillation detectors,” *Phys. Med. Biol.*, vol. 57, no. 7, pp. 1797–1814, 2012.
- [40] H. H. Barrett and K. J. Myers, *Foundations of Image Science*. Wiley, 2004.
- [41] J. Perl, J. Shin, J. Schümann, B. Faddegon, and H. Paganetti, “TOPAS: An innovative proton Monte Carlo platform for research and clinical applications,” *Med. Phys.*, vol. 39, no. 11, pp. 6818–6837, 2012.
- [42] C. Z. Jarlskog and H. Paganetti, “Physics settings for using the Geant4 toolkit in proton therapy,” *IEEE Trans. Nucl. Sci.*, vol. 55, no. 3, pp. 1018–1025, 2008.
- [43] J. Smeets *et al.*, “Prompt gamma imaging with a slit camera for real-time range control in proton therapy,” *Phys. Med. Biol.*, vol. 57, no. 11, pp. 3371–3405, 2012.
- [44] E. Lens, T. Z. Jagt, M. S. Hoogeman, and D. R. Schaart, “Correlations between the shifts in prompt gamma emission profiles and the changes in daily target coverage during simulated pencil beam scanning proton therapy,” *Phys. Med. Biol.*, vol. 64, no. 8, p. 085009, 2019.